

## RESEARCH ARTICLE

10.1002/2013JB010475

## Key Points:

- Large displacements (>40 cm) and accelerations (~1g) in 10 Hz GPS records
- Conventional and less conventional amplification mechanisms are evaluated
- A low-velocity fault zone model is found to best fit GPS records

## Supporting Information:

- Readme
- Figure S1
- Figure S2
- Figure S3
- Figure S4
- Table S1

## Correspondence to:

A. Avallone,  
antonio.avallone@ingv.it

## Citation:

Avallone, A., A. Rovelli, G. Di Giulio, L. Improta, Y. Ben-Zion, G. Milana, and F. Cara (2014), Waveguide effects in very high rate GPS record of the 6 April 2009,  $M_w$  6.1 L'Aquila, central Italy earthquake, *J. Geophys. Res. Solid Earth*, 119, 490–501, doi:10.1002/2013JB010475.

Received 27 JUN 2013

Accepted 12 DEC 2013

Accepted article online 17 DEC 2013

Published online 21 JAN 2014

## Waveguide effects in very high rate GPS record of the 6 April 2009, $M_w$ 6.1 L'Aquila, central Italy earthquake

Antonio Avallone<sup>1</sup>, Antonio Rovelli<sup>2</sup>, Giuseppe Di Giulio<sup>3</sup>, Luigi Improta<sup>2</sup>, Yehuda Ben-Zion<sup>4</sup>, Giuliano Milana<sup>2</sup>, and Fabrizio Cara<sup>2</sup>

<sup>1</sup>Istituto Nazionale di Geofisica e Vulcanologia, Centro Nazionale Terremoti, Rome, Italy, <sup>2</sup>Istituto Nazionale di Geofisica e Vulcanologia, sezione di Roma1, L'Aquila, Italy, <sup>3</sup>Istituto Nazionale di Geofisica e Vulcanologia, sezione di Roma1, L'Aquila, Italy, <sup>4</sup>Department of Earth Sciences, University of Southern California, Los Angeles, California, USA

**Abstract** A 10 Hz sampling frequency GPS station was installed near L'Aquila a few days before the 6 April 2009  $M_w$  6.1 earthquake. It recorded displacement waveforms during the main shock and the largest  $M_w$  5.4 aftershock of 7 April. The horizontal components of the main shock contain a high-amplitude (43 cm peak-to-peak) nearly harmonic (1 Hz) wave train not evident in other nearby instrumental records. The persistency of this feature during aftershocks recorded by a temporarily colocated seismological station highlights a local site effect. Traditional models based on near-surface velocity structure and topography variations fail to reproduce the size and frequency band of the observed amplified motion. The amplified wave train can be explained by a low-velocity fault zone layer below the station. This model fits the delay of the large-amplitude nearly harmonic wave train after the *S* wave phase and is consistent with the variation in the fault excitation efficiency between the two shocks in relation to their different source depth and location. Synthetic calculation of trapped waves in a model consisting of two quarter spaces separated by a 650 m wide low-velocity zone with 50% velocity reduction and *Q* value of 20 fit well the observed anomalous record. The parameters of the model fault zone layer are consistent with geological evidence of a broad damage zone adjacent to the station and a similar site response found in this crustal zone with ambient noise. Results of shallow seismic surveys and sonic logs from deep wells provide independent constraints on the host rock velocities.

### 1. Introduction

On 6 April 2009, at 01:32 UTC, central Italy was struck by a  $M_w$  6.1 earthquake [Scognamiglio *et al.*, 2010] causing about 300 casualties and extensive damage in the L'Aquila town and in several nearby villages (Figure 1). The main shock was preceded by a preseismic sequence with the largest ( $M_w$  4.1) foreshock occurring 1 week before, and it was followed by a  $M_w$  5.4 shock on 7 April to the southeast and by a  $M_w$  5.2 shock on 9 April to the north (Figure 1). The three  $M_w > 5$  strongest shocks were followed by a long aftershock sequence [Chiaraluce *et al.*, 2011; Valoroso *et al.*, 2013, and references therein]. The region is known to be highly active seismically as documented in historical [Working Group Catalogo Parametrico dei Terremoti Italiani, 2004] and instrumental [Chiarabba *et al.*, 2005] catalogs. The main shock epicenter was located a few kilometers southwest of the town of L'Aquila [Chiarabba *et al.*, 2009] and the focal mechanism (Figure 1) suggests that the main shock occurred on a NW-SE striking and 50°SW dipping normal fault [Scognamiglio *et al.*, 2010], whose surface projection corresponds to the Paganica fault [Bagnaia *et al.*, 1992; Boncio *et al.*, 2004]. This mechanism is in agreement with the NE-SW direction of the crustal extension in the Central Apennines, amounting to 2.5–3 mm/yr in a 40–50 km wide belt [D'Agostino *et al.*, 2011]. The GPS-derived static offsets [Anzidei *et al.*, 2009; Cheloni *et al.*, 2010] and the deformation field obtained by InSAR (Interferometric Synthetic Aperture Radar) [Atzori *et al.*, 2009; Walters *et al.*, 2009] have been used, separately [Cheloni *et al.*, 2010; Cirella *et al.*, 2012; Serpelloni *et al.*, 2012] and jointly [Trasatti *et al.*, 2011; Cirella *et al.*, 2012; D'Agostino *et al.*, 2012], to obtain the coseismic slip distribution on the causative fault. In addition, the kinematic rupture process of the earthquake was determined by a joint inversion of the geodetic results combined with the strong ground motion data [Cirella *et al.*, 2009, 2012] and with the high-rate (10 Hz and 1 Hz) GPS (HRGPS) time series in the near field [Avallone *et al.*, 2011]. The data recorded by the HRGPS CADO site (Figure 1) provided satisfactory ground displacement waveforms for the two largest shocks and is the focus of the present study.

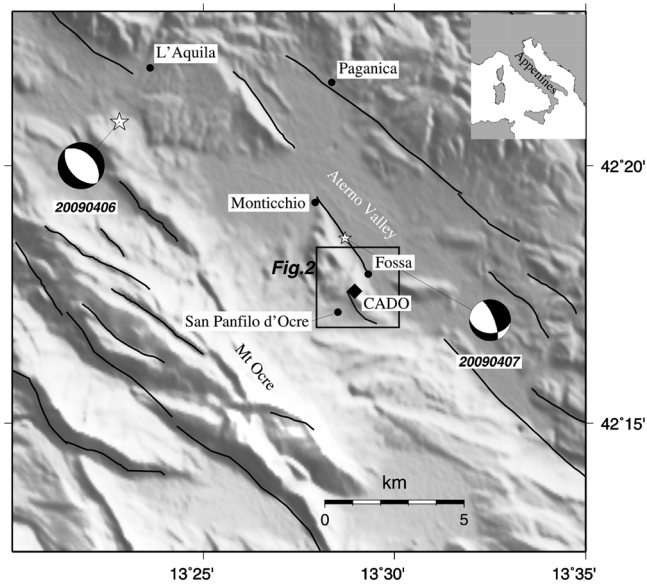


**Figure 1.** Location map of the area associated with the L'Aquila earthquake. Black lines correspond to the main active faults around the city of L'Aquila [Boncio *et al.*, 2004; Roberts and Michetti, 2004; Galli *et al.*, 2008; EMERGEO Working Group, 2009; Boncio *et al.*, 2010; Foglio CARG, 2009]. The white stars and the “beach balls” show the locations [Chiarabba *et al.*, 2009] and the focal mechanisms [Scognamiglio *et al.*, 2010] of the main shock ( $M_w$  6.1 on 6 April 2009) and of the strongest aftershock ( $M_w$  5.4 on 7 April 2009), respectively. The black diamond represents the position of the CADO high-rate GPS site. The black square indicates the area represented in Figure 2.

The CADO HRGPS is installed on a cliff close to a complex faulting system located at the eastern margin of the Mount Ocre ridge. In the CADO record of the main shock, Avallone *et al.* [2011] noted the presence of a nearly harmonic high-amplitude displacement wave train several seconds after the beginning of the dynamic deformation. In the following sections we describe the three-dimensional motion recorded at CADO and investigate the possible origin of this high-amplitude wave train. We show that conventional models of site effects cannot capture the unusual signal at the CADO record. We demonstrate with synthetic waveform calculations that the anomalous large-amplitude signal can be generated as a consequence of a seismic trapping structure below the station. Vibrations of large rock blocks can also contribute to the examined signal.

## 2. Local Site Conditions of CADO

The site CADO is on the crest of a narrow ridge which is elongated in the NW-SE direction and bounds the Aterno Valley to the west (Figure 1). In particular, the site is about 50 m from a cliff associated with the NE dipping normal fault of Monticchio-Fossa (Figures 1–3). The western slope of the ridge is in turn crosscut by a system of NW-SE trending and SW dipping Quaternary normal faults. One of these faults is a few tens of meters from the GPS site which lies in the footwall side on limestones (Figure 2). The ridge is formed by shelf limestones (Mesozoic-Miocene) and by thin flysch sequences (Upper Miocene), which are exposed (Figure 2) in the footwall and in the hanging wall side of the western fault system, respectively [Foglio CARG, 2009]. These shelf carbonates were stacked and deeply deformed during the Mio-Pliocene compressional tectonic phases [Ghisetti and Vezzani, 1997] and subsequently dissected during Quaternary extension that generated normal fault systems and reactivated inherited structures [Galadini, 1999].

Due to the intense deformation related to thrust tectonics and normal faulting, limestones in the area are highly fractured. Along the ridge, this is reflected by several dolines that document intense karst processes and quarries exploiting the highly fractured limestones outcrops (Figure 3). Sonic logs from deep wells (UNMIG well database, <http://unmig.sviluppoeconomico.gov.it/vidempi/en/gpozzi.htm>) provide the following reference  $P$  wave velocity ranges for sedimentary sequences in the region: 5.5–6.0 km/s for Mesozoic shelf limestones, 4.7–5.5 km/s for Miocene limestones, and 3.5–4.0 km/s for Upper Miocene flysch deposits. High-resolution tomography surveys performed across the Aterno Valley, 3 km to the NE of CADO, indicate

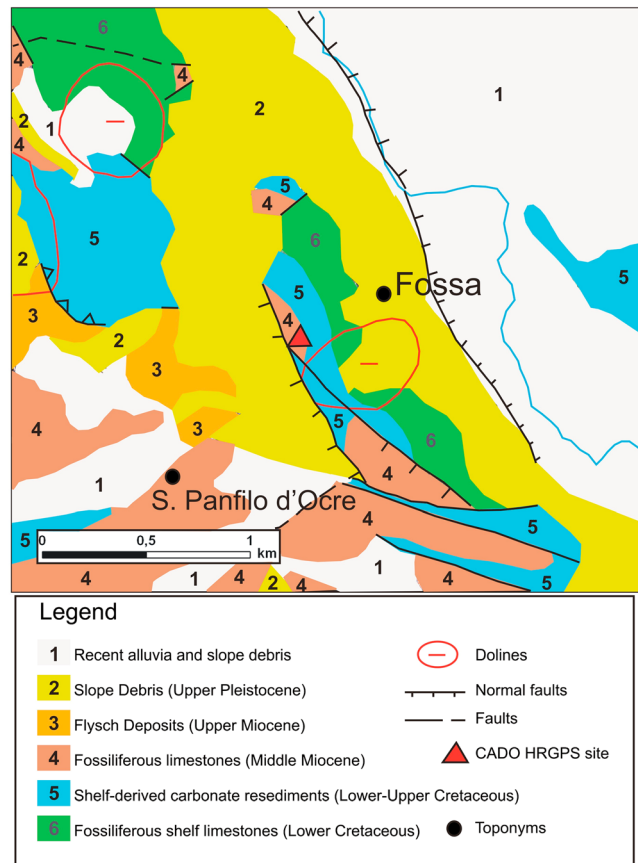


**Figure 2.** Simplified geologic map focused on the Fossa–San Panfilo d’Ocre area (Figure 1) (modified from the *Foglio CARG* [2009]). The numbers and colors represent the different lithologies described in the legend below.

considerably lower *P* wave refraction velocities with respect to the well data: 4.0–4.5 km/s for the Mesozoic–Miocene limestones and 3.2–3.5 km/s for the Miocene flysch imaged at 200–500 m depth below the Quaternary sediments of the Aterno basin [*Improta et al., 2012*]. These low *P* wave refraction velocity values were ascribed to fractured carbonate rocks.

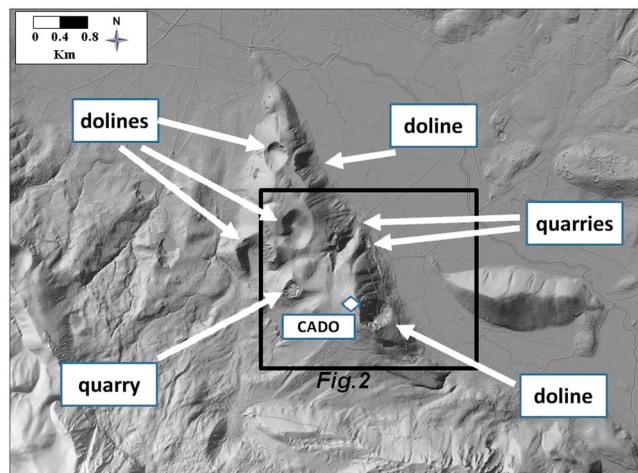


**Figure 3.** A 1 m resolution LIDAR (Laser Imaging Detection and Ranging) image (modified from *Civico et al. [2013]*) highlighting the dolines and quarries of the investigated area. The black square indicates the area represented in Figure 2.

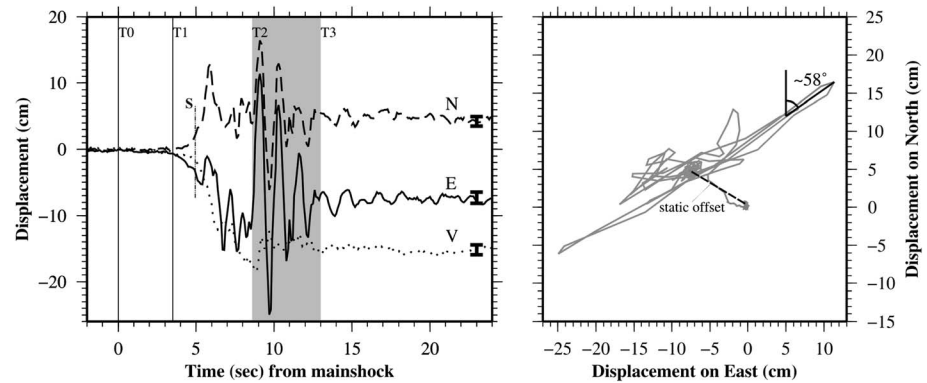


**Figure 4.** (left) HRGPS time series at CADO (modified from *Avallone et al.* [2011]). The dashed, solid, and dotted lines represent the North, East, and Vertical components, respectively, with relative  $2\sigma$  noise levels represented by the error bars. The two vertical lines (T0 and T1) represent the time of the main shock occurrence [*Chiarabba et al.*, 2009] and of the starting of the dynamic coseismic displacement, respectively, whereas the background grey area corresponds to the time between the beginning (T2) and end (T3) of the nearly harmonic high-amplitude phase. The S vertical line represents the arrival time of the S wave. (right) Particle motion of the CADO coseismic dynamic displacement in the horizontal plane; the dashed line represents the static horizontal offset occurred between the time intervals T1 and T3 of Figure 4 (left).

### 3. Analysis of the 3-D High-Rate GPS Motion of CADO

The L'Aquila main shock was recorded by a number of continuous HRGPS stations, belonging to the Rete Integrata Nazionale GPS (RING, <http://ring.gm.ingv.it>) and to other regional networks [*Avallone et al.*, 2011]. After the occurrence of the largest foreshock ( $M_w$  4.1 on 31 March 2009), a few days before the main shock, some survey-style GPS benchmarks were also installed [*Anzidei et al.*, 2009]. For two of these benchmarks the receivers were set up with a 10 Hz sampling frequency. Here we focus on data recorded at the CADO HRGPS site (Figure 1). The analysis of CADO data by *Avallone et al.* [2011] yields  $2\sigma$  noise levels of 0.72, 0.86, and 0.76 cm for the North, East, and Vertical components, respectively (Figure 4, left).

The HRGPS time series at CADO indicates that the earthquake-related deformation (T1) starts about  $3.5 \pm 0.1$  s after the event rupture nucleation (T0) (see Figure 4, left). The vertical component clearly shows a subsidence that occurred in three steps. The projection of the 3-D particle motion (Dynamic Content S1 in the supporting information) indicates that in the first  $5.1 \pm 0.1$  s of the coseismic dynamic displacement the CADO motion is mainly dominated by a subsidence related to the fault slip. This subsidence can be divided into two phases. The first one, spanning  $1.1 \pm 0.1$  s, shows the S wave arrival (S) and describes a low-dipping ( $\sim 15\text{--}20^\circ$ ) subsidence in the NW direction (first step) which reaches almost half of the final static offset on the horizontal components. The second phase, spanning  $4.0 \pm 0.1$  s, describes a mainly vertical two-steps motion accompanied by oscillations on the East component with amplitudes of  $\sim 10$  and  $\sim 5$  cm. At the end of this phase (T2), about  $5.1 \pm 0.1$  s after the initial motion (T1) (Figure 4, left), the vertical component has reached a value (17.7 cm) larger than the final coseismic displacement (15 cm). Starting from T2,  $4.0 \pm 0.1$  s after the S wave arrival, the horizontal records at CADO have a strong oscillatory wave train, whereas the vertical component shows an upward movement till its final static value. This wave train starts with a pulse having a very high peak-to-peak amplitude totaling 36.4 cm in the east component and 22.6 cm in the north component (Figure 4, left). The large initial pulse is followed by a number of nearly harmonic (around 1 Hz) cycles that decrease in amplitude and reach the final static horizontal offset after  $4.4 \pm 0.1$  s (T3). The particle motion in the horizontal plane (Figure 4, right) shows that the high-amplitude displacement totals 42.8 cm and mainly occurs in the  $\sim N58^\circ E$  direction, fairly normal to the fault strike and to the direction of the static offset.

## 4. Origin of the High-Amplitude Nearly Harmonic Wave Train

### 4.1. Evidence of a Site Effect

*Avallone et al.* [2011] inferred a kinematic rupture model of the 6 April main shock through a joint inversion of GPS-derived static offsets, strong motion data, and HRGPS time series. They showed that the high-amplitude ground motion in the time window T2–T3 is not reproduced in the frequency range 0.02–0.5 Hz. Therefore, an alternative interpretation in terms of propagation effects is sought.

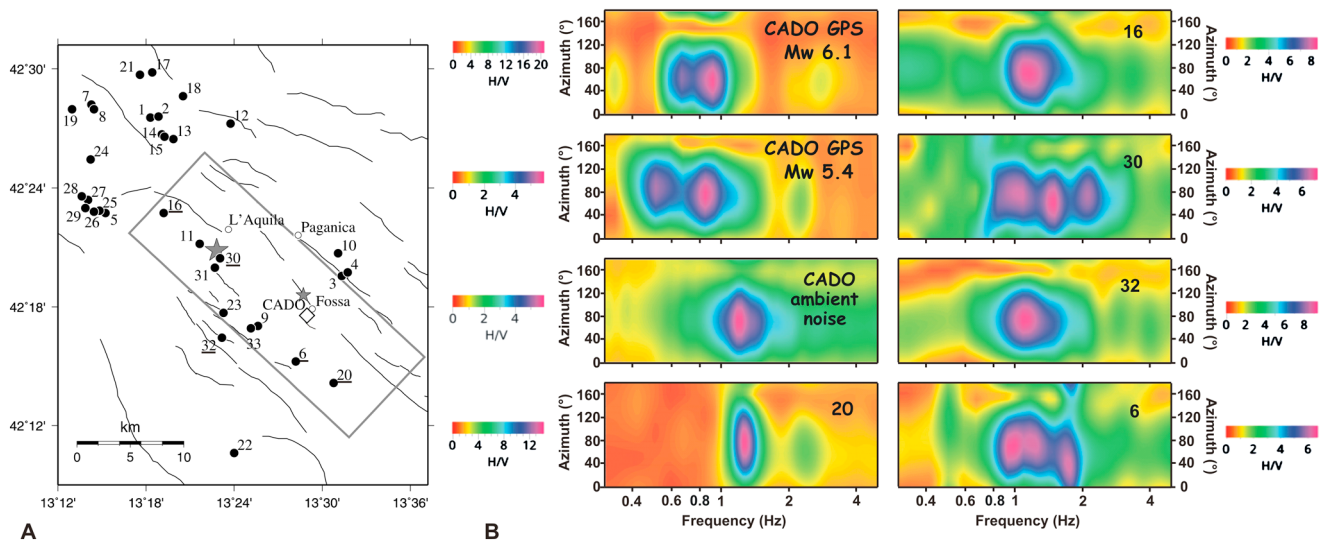


**Figure 5.** (a) Location of the aftershocks (black circles) recorded by the seismological station installed from April to July 2010, a few meters from the GPS antenna (white diamond). The larger and smaller grey stars represent the epicenters of the main shock and of the largest aftershock, respectively. The grey box indicates the surface projection of the previously proposed finite fault model [Cirella et al., 2009; Avallone et al., 2011]. (b) The color contour plots are the HVSr of the rotated horizontal components of different types of signals: for the main shock and the largest aftershock using the GPS waveforms, as well as for ambient noise and some aftershocks (underlined identification numbers in Figure 5a: 6, 16, 20, 30, and 32) aftershocks closest to the ruptured fault using the seismological records.

The GPS monumentation at CADO consists of a 1.5 m tall concrete pillar, on which the GPS antenna was screwed and further fixed using cement (Figure S1 in the supporting information). One year after the L'Aquila earthquake a seismological station equipped with a 5 s velocity transducer was installed a few meters from the GPS benchmark. The main goals of this installation were to check the consistency of the response of the GPS antenna with a free-field colocated instrument and to investigate the possible existence of site-dependent systematic effects during earthquakes.

Many small-magnitude ( $M < 3$ ) earthquakes were recorded during the acquisition of the colocated seismological station between 23 April 2010 and 31 July 2010 (Figure 5). Details on these aftershocks are listed in Table S1. Consistently with the GPS trace, the waveforms of the aftershocks located near the main shock hypocenter show amplitudes and durations greater in the horizontal components than in the vertical one (Figure S2). Important insights come from the horizontal-over-vertical spectral ratio (HVSr) of rotated horizontal components. The HVSrs are calculated by rotating the horizontal components with steps of  $10^\circ$  in the range  $0^\circ$ – $180^\circ$  [Spudich et al., 1996] and, for each step, by dividing the horizontal spectrum with the vertical spectrum. This is done for the GPS trace of the main shock and the  $M_w$  5.4 aftershock, as well as for other aftershocks seismograms and for an ambient noise record (Figure 5).

The HVSrs versus frequency and azimuth shown in Figure 5 were computed using the GEOPSY software (<http://www.geopsy.org>) after applying to the data a high-pass filter at 0.5 Hz. The GEOPSY software is a tool suited for microtremor analysis [Bard et al., 2010]. We used a time window of 12 s for the GPS and aftershock recordings bracketing the most energetic part of the time histories, and the Fourier amplitude spectra were smoothed with a Konno and Ohmachi [1998] filter using a coefficient of 20 for the bandwidth. For the ambient noise analysis of the temporarily colocated seismological station, the HVSrs of Figure 5 were computed using 60 time windows of 60 s duration after removing nonstationary disturbances using the antitrigger option of GEOPSY that is based on a short-term average over long-term average ratio. We finally checked that analyzing noise records in different time periods does not change the shape of the HVSrs curve.

The results of Figures 5 and S2 indicate that the site is responsible for a significant amplification of horizontal ground motion around 1 Hz compared to the vertical component. Usually, amplification is estimated through spectral ratios relative to a reference site; however, in this case the lack of a reference site led us to use HVSrs as a proxy. In Figure 5 we see that the 1 Hz amplification is independent of the source and nature of the signal (weak and strong motions along with ambient noise in GPS and seismic instruments) and is strongly directional with amplitudes of HVSrs being much larger at an azimuth of about  $60^\circ$  from North, roughly transversal

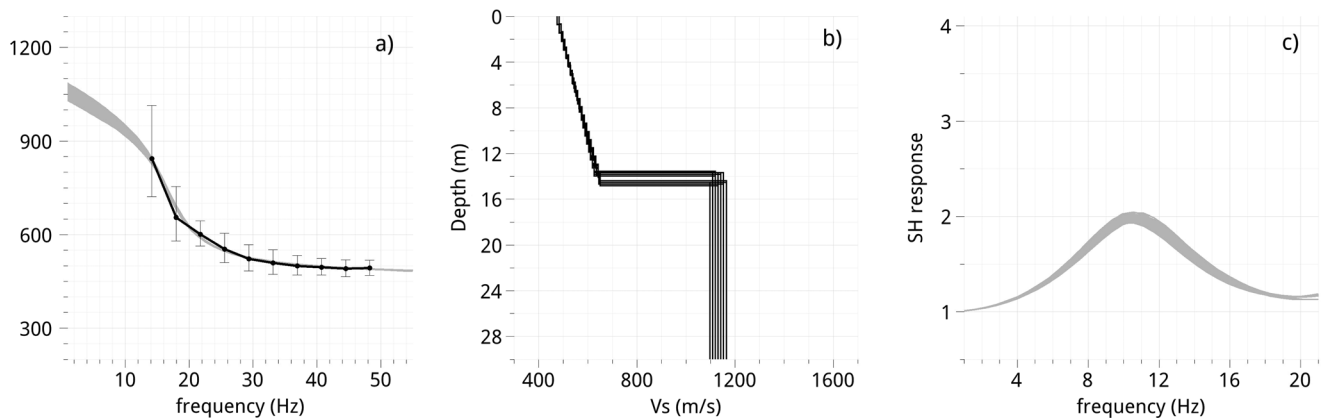


**Figure 6.** (a) Dispersion of Rayleigh waves obtained from active seismic experiments. The black curve with standard deviation is inferred from the MASW analysis, whereas the grey band corresponds to the range of all dispersion curves of the best fitting models. (b)  $V_s$  profiles derived from the inversion of Figure 6a. (c) SH transfer functions for the best fitting models.

to the strike of the faults in the region. This is a clear indication that independently of the possible source contribution, the high-amplitude horizontal displacement has to be ascribed primarily to a site-dependent propagation effect.

The outcropping rocks are limestones, although fractured and weathered, so a significant site effect caused by a thick soft upper layer is not possible. Vertical velocity profiles of the uppermost layers were assessed during the NERA (Network of European Research infrastructures for earthquake risk Assessment and mitigation) Project [Rovelli *et al.*, 2013, <http://www.nera-eu.org/>] through ultrashallow active experiments using the MASW (multichannel analysis of surface waves) technique. These seismic experiments yield a 1-D shear wave profile through the inversion of the dispersion curves of Rayleigh waves (Figure 6).

The result suggests that the near-surface degradation of rock affects the uppermost 15 m with velocities ranging from 500 to 650 m/s. Below this shallow layer, the velocities are of the order of 1000 m/s with an impedance contrast of about 2. This feature rules out a significant amplification around 1 Hz since the transfer function of this 1-D model only produces a small amplification around 10 Hz.

#### 4.2. Topographic Effect

As mentioned, the HRGPS and the colocated seismological station are located at the edge of a cliff, a few tens of meters from the slope break (Figure 3), with a variation of elevation by 350 m and a steep (about 30°) slope. Strong topography variations are known to cause local amplifications [Spudich *et al.*, 1996; Geli *et al.*, 1988; Lee *et al.*, 2009; Buech *et al.*, 2010; Pischiutta *et al.*, 2010]. The possible role of topography on the GPS waveforms has been investigated using a 2-D model with the following elastic and anelastic parameters:  $S$  and  $P$  wave velocities of 1000 and 2000 m/s, respectively, quality factors  $Q_S$  and  $Q_P$  (obtained simply dividing the velocities by 10) of 100 and 200, respectively, and mass density of  $2.5 \text{ g/cm}^{-3}$ . Constraints on the velocities of this model come from the MASW experiments (Figure 6). For simplicity, the relief is modeled as having uniform rock properties and the adjacent Aterno basin is not included in the model, as the analysis is focused on the role of the free surface lateral variations. The seismic response of the Mount Ocre topography to delta-like Gabor seismic input was simulated through the code Web Interface for Seismological Applications (WISA) that uses a finite-element approach with visco-elastic linear rheology [Caserta *et al.*, 2002; Ruggiero *et al.*, 2004] and a user-friendly web interface to insert the corresponding 2-D model [Santoni *et al.*, 2004].

The P-SV propagation was modeled for a vertically incident (in-plane) horizontally polarized pulse and the 2-D simulations were made in the time domain. The numerical model with WISA uses a triangle mesh generator (<http://www.cs.cmu.edu/~quake/triangle.html>). Our simulation provides reliable results up to 8 Hz. Using synthetic seismograms, the propensity of the topographic irregularity to amplify ground motion along the profile is estimated using spectral ratios with respect to a reference site, which is the synthetic seismogram of the same model without topography. These spectral ratios (Figure 7) show that the lateral variations of the free surface cause ground motion amplification at high frequency ( $f > 5 \text{ Hz}$ ) and the effect is smaller than a factor of 2 around 1 Hz. Although the modeling is very simple (2-D and uniform rock), the numerical simulations suggest that the peculiar high-amplitude wave train around 1 Hz cannot be produced by the lateral variations of topography. If the model

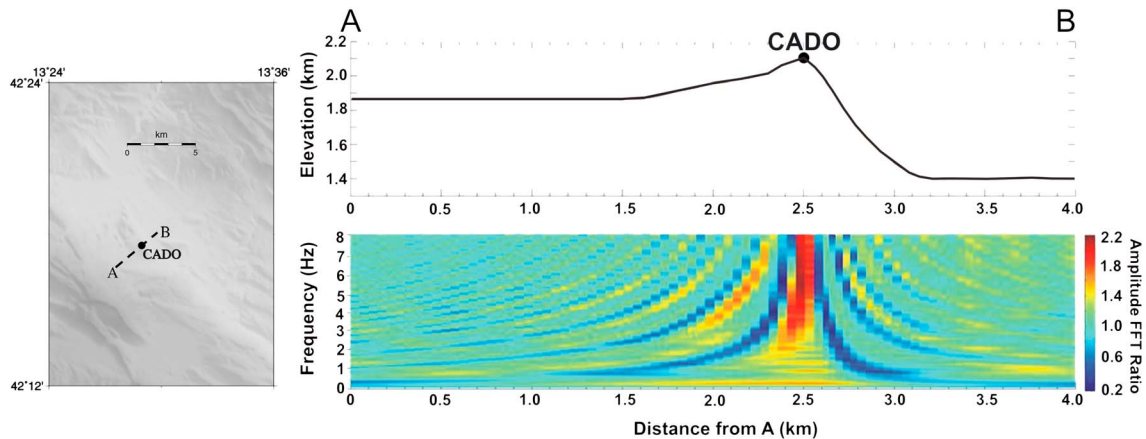


**Figure 7.** (left) Location map of the profile AB used in the topographic simulations (dashed line). (right top) Topographic profile AB of the Mt. Ocre easternmost flank. The black dot indicates the position of CADO on the profile AB. (right bottom) Color palette quantifying the amplification along the topography as a function of frequency as estimated through the numerical modeling.

velocities are reduced by a factor of 2 (not shown in figure) the amplification pattern does not change significantly in amplitude and peaked frequencies, suggesting that no realistic velocity value can yield theoretical results comparable to observations when uniform rock models are adopted.

Other possible mechanisms of amplification on mountains have been recently proposed in the literature [Marzorati *et al.*, 2011; Moore *et al.*, 2011; Burjáněk *et al.*, 2012]. These authors ascribe the large directional horizontal motions to resonance of fractured rock blocks on unstable slopes. Similarly to our observations, in those papers the largest motions are transversal to the fracture orientation. Although a similar mechanism could be in principle invoked for the high-amplitude horizontal motions of CADO, there is a critical difference. These large horizontal motions are expected to occur as an amplification of the whole seismic signal, whereas Avallone *et al.* [2011] demonstrated that the direct *S* waves of CADO are well fit by the rupture source model. In the examined data, the 1 Hz amplification is limited to a time window that begins 4.0 s after the *S* wave arrival (Figure 4, left). For this reason a resonance of rock blocks does not seem to be fully convincing, leading us to explore one more possible amplification mechanism.

### 4.3. Waveguide Effect

The local geologic conditions around CADO suggest the existence of a low-velocity damage zone (Figure 3) associated with SW dipping normal faults located a few tens of meters to the west from the GPS site (Figure 2). This suggests a possible interpretation of the high-amplitude wave train in terms of a waveguide effect near the station. To examine the plausibility of this mechanism we fit the fault-parallel component of the HRGPS high-amplitude wave train with synthetic calculations of fault zone-trapped waves. The synthetic waveforms are generated using the analytical solution of Ben-Zion and Aki [1990] for an SH line dislocation (i.e., slip parallel to the fault zone and the free surface) in a structure consisting of a low-velocity vertical fault zone layer between two quarter spaces (Figure 8).

First, we constrained some parameters using independent data, such as the velocity value of the left quarter space, the position of the GPS receiver in the fault zone and the source-receiver distance. Based on field geological data (Figure 2), *P* wave refraction velocities of 4000–4500 m/s estimated for shallow fractured limestones [Improta *et al.*, 2012] and assuming a  $V_p/V_s$  value of 1.9, the *S* wave velocity has been fixed at 2200 m/s (and accordingly a *Q* of 250 is used). This value is consistent with a high  $V_p/V_s$  anomaly found in the shallow crust (0–3 km depth) beneath the Aterno Valley by Di Stefano *et al.* [2011] and it is indicative of fractured and water-saturated carbonates. The position of the GPS receiver is fixed close to the right interface of the fault zone, roughly at the edge of the damage zone outlined by dolines and visible in Figure 3. This is also consistent with the fact that we expect a higher fracturing of the limestones in the hanging wall side of the nearby normal faults [Berg and Skar, 2005]. To estimate the source-receiver distance, we considered the largest slip patch of the kinematic rupture model of Cirella *et al.* [2009] and Avallone *et al.* [2011]. This largest patch was activated about 2 s after the nucleation and ~8 km to the SE; it reaches a maximum slip of about

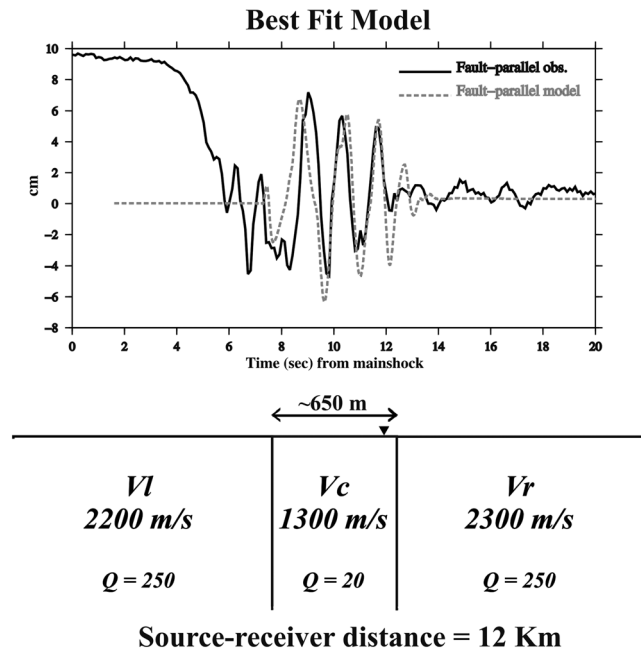


**Figure 8.** (top) Synthetic waveform fit of the CADO fault-parallel displacement component. To take into account the considerable coseismic static offset, the fault-parallel component has been vertically shifted to better compare the observed and modeled trends. (bottom) A sketch diagram of the fault model.

1.1 m about 1.5 s later and ~3 km to the NW from CADO, at depths of 11–12 km beneath. Thus, a source-receiver distance of 12 km appears to be reasonable for the main shock.

Second, using the above values of the S wave velocity and Q for the left quarter-space of Figure 9, the position of the receiver and the source-receiver distance of 12 km, we fit the large-amplitude wave train. The fit is obtained with a simple trial-and-error approach. The minimum misfit between the synthetic and the observed waveforms (Figure 8) is found for the following model parameters: width of low-velocity fault zone of 650 m; S wave velocity and Q value of the fault zone of 1300 m/s and 20, respectively; S wave velocity and Q of the right quarter-space of 2300 m/s and 250, respectively. As shown in Figure 8, these parameters lead to satisfactory modeling of both the amplitudes and phases of the observed large-amplitude oscillatory record. A satisfactory fit is also obtained for the 7 April aftershock using the velocity structure of Figure 8 (Figure S3).

### 5. Discussion

The model used to calculate the synthetic waveforms has a small number of parameters that affect significantly the generated guided waves. These are essentially the seismic velocity contrast of the fault zone layer with the surrounding blocks, Q value of the fault zone and the ratio of propagation distance within the fault zone layer divided by the fault zone width [Ben-Zion and Aki, 1990; Ben-Zion, 1998]. Some parameters are constrained by independent data, as mentioned, and the other parameters leading to the waveform fit of Figure 8 have reasonable values. The model simplicity and good obtained fit to the observed data suggest that the large-amplitude anomalous record at CADO is produced at least partially by a waveguide effect. There is inherent nonuniqueness in the model results related to trade-off among model parameters [Ben-Zion, 1998], but constraining some parameters independently as done here reduces considerably from the nonuniqueness.

The interpretation of the model parameters requires caution. The velocity and Q values of the bounding blocks are assumed to represent average properties of the top few km sequence of the overlapped carbonate thrust sheets outcropping in the area. The obtained best fitting model parameters are consistent with independent information. The width of the low-velocity block (about 650 m) is consistent with the extension of the zone inferred by the distribution of dolines on the carbonate ridge. Shear wave velocity values of the right block of Figure 8 are compatible with P wave velocities determined for the limestones underneath the Aterno

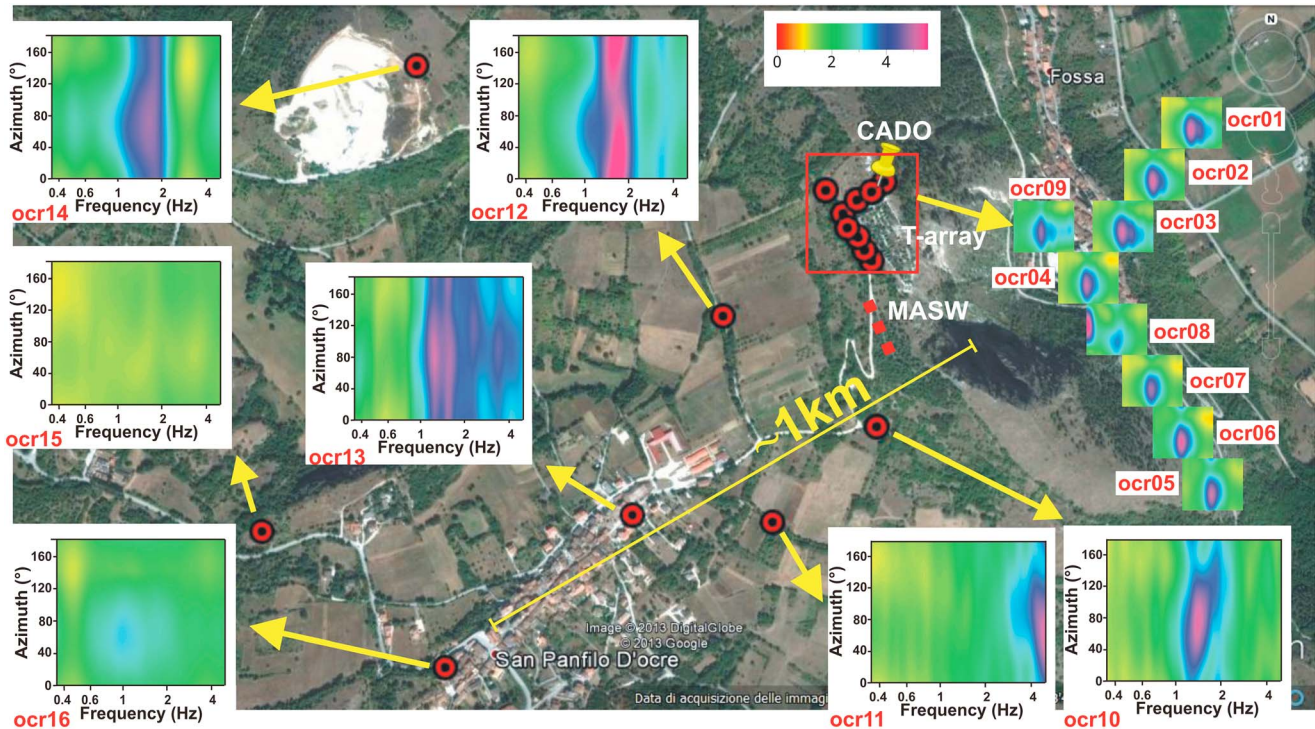


**Figure 9.** Results of ambient noise measurements (red circles) performed in the study area. The T-array HVSR plots have the same axis ranges as the other HVSR plots shown in figure, but they have been removed for clarity. There is significant stability of the directional spectral peak up to hundreds of meters from CADO (yellow marker), and the 1 Hz peak tends to disappear at distances of the order of 1000 m.

valley by refraction tomography [Improta et al., 2012] and with high  $V_p/V_s$  values imaged in the shallow crust [Di Stefano et al., 2011]. The extremely low  $S$  wave velocity value of the fault zone is in agreement with results of the active seismic experiment (MASW) carried out around the CADO site and with the presence of highly fractured and karst-weathered limestones. Those velocity values as well as the source-receiver distance provide a time delay ( $\sim 4$  s) of the modeled high-amplitude signal (Figure 8) that is consistent with the time delay between the  $S$  wave arrival and the beginning of the high-amplitude pulse in the observations ( $S$  and  $T_2$ , respectively, in Figure 4 left).

The existence of a wide damage zone with a seismic response similar to that of CADO is confirmed by measurements of ambient noise in the crustal region adjacent to CADO. Although a large part of the area is not accessible because of topographic variations and the accessible part is cultivated (therefore having in many places soft soil outcrop), the ambient noise recorded at stiff sites (Figure 9) shows that the HVSRs maintain the spectral signature of CADO for hundreds of meters to the SW of the GPS station, consistent with the best fitting model. This feature decreases in intensity at locations with larger distances from CADO: the 1 Hz peak tends to disappear at distances on the order of 1000 m.

The validity of a fault zone excitation model is supported also by the different behavior of CADO during the two strongest shocks of the L'Aquila seismic sequence and similarity of the anomalous features in the CADO record to other observations involving fault zone-trapped waves. Both the nucleation of the largest slip patch related to the main shock [Cirella et al., 2009; Avallone et al., 2011] and the hypocenter of the  $M_w$  5.4 aftershock [Chiaraluce et al., 2011] occurred roughly beneath the CADO GPS site but at slightly different depths:  $\sim 12$  km for the main shock and  $\sim 15$  km for the aftershock. Figure 10 shows a comparison of the CADO fault-transversal component between the two events in terms of ground displacement (Figure 10a) and ground acceleration (Figure 10b). Both horizontal ground displacements and accelerations differ by a factor of 10 between the two events. Note that the ground acceleration time series attained  $\sim 1$  g during the main shock in spite of the limited bandwidth (5 Hz), a value considerably larger than peak ground acceleration (PGA) of all the nearby strong motion accelerometers that range between 0.3 and 0.6 g [Çelebi et al., 2010]. Similar large

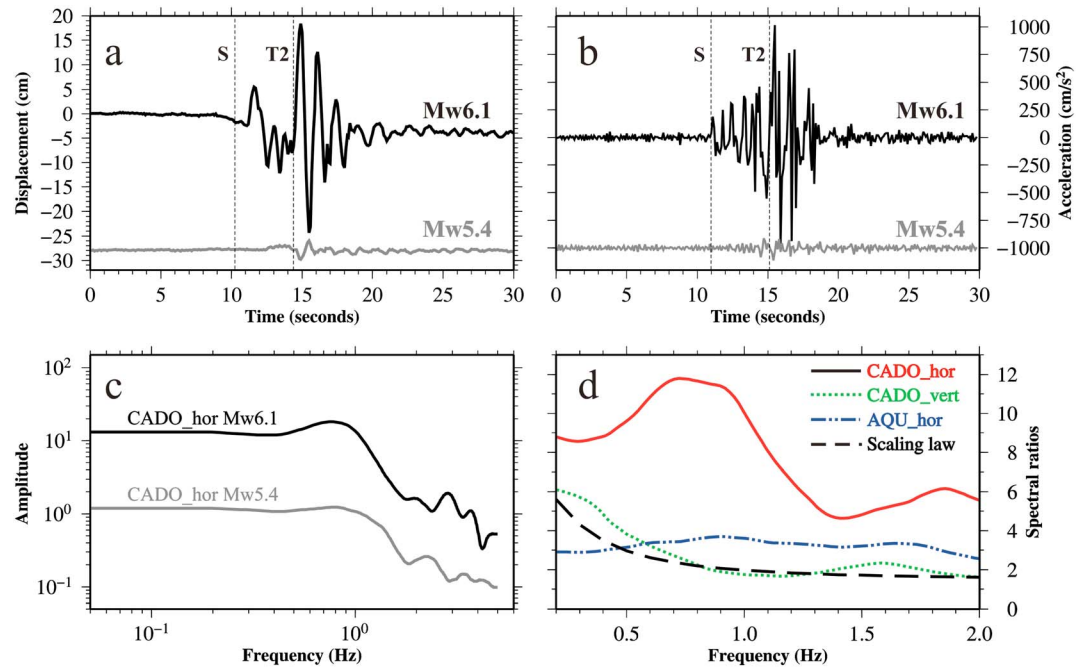


**Figure 10.** Comparison of (a) fault-transversal ground displacements and (b) ground accelerations recorded at CADO during the  $M_w$  6.1 on 6 April 2009 main shock (black trend) and the  $M_w$  5.4 on 7 April 2009 aftershock (grey trend). (c) Black and grey trends correspond to the spectral amplitudes of the fault-normal CADO components for the main shock and aftershock, respectively. (d) The spectral ratio of the horizontal motion of CADO (red continuous line) is compared to the spectral ratio of the vertical component of CADO (green dotted line) and the horizontal motion of AQU (blue dash-dotted line). For reference, the expected scaling law is superimposed (black dashed line) using spectral parameters of Calderoni *et al.* [2013]. The spectral ratios are corrected for the distances of AQU and CADO from the sources.

PGA and motion amplification were observed at a fault zone site above a trapping structure at the North Anatolian Fault [Seeber *et al.*, 2000; Ben-Zion *et al.*, 2003; Peng and Ben-Zion, 2006].

The large difference in amplitude between the two events is in contrast with the expected scaling based on seismic moments and stress drops. Calderoni *et al.* [2013] estimated 9 and 17 MPa for the  $M_w$  6.1 and 5.4 shocks, respectively; therefore, the much larger amplitude of the main shock cannot be due to a larger stress drop of the main shock. Horizontal ground motion spectra of the two events (shown in Figure 10c) are very coherent between 0.2 and 2 Hz, which is the frequency band of the nearly harmonic excitation observed at CADO. Above 2 Hz, spectral bumps and holes occur at different frequencies in the spectra of the two events. Examining the largest coherence frequency band 0.2–2 Hz, we see that the spectral ratio of the maximum amplitude component between the two events is far from the spectral-scaling expectation (the smooth curve of Figure 10d). In contrast, both the vertical components of CADO and horizontal motions of the nearest strong motion accelerograms in the town of L’Aquila (AQU, around 10 km from CADO) are satisfactorily fit by the theoretical source scaling. This means that a strong propagation/site-related mechanism caused a different amplification of the horizontal motion during the two events. Three-dimensional numerical calculations of Fohrmann *et al.* [2004] show that the strength of excitation of trapped fault zone waves depends strongly on the distance and orientation of the radiating source with respect to the low-velocity fault zone layer. Due to the different source depth, a different coupling with the resonant fault zone is likely the reason for the generation of oscillatory waveform with strong amplification during the shallower event.

### 6. Concluding Remarks

The nearly harmonic large-amplitude signal at the HRGPS CADO station appears to result from (i) the location of the GPS site with respect to the source, above the causative fault and, in particular, above the largest slip patch and (ii) the location of the GPS site with respect to the geological structure, within a crustal damage zone characterized by highly fractured limestones. The recording of the signal was made possible by the high sampling frequency (10 Hz) at the GPS station, which is considerably higher than the traditional acquisition rates (30 s or 1 s). The combination of all these effects was responsible for a ground acceleration of the order

of 1 g at the CADO site, and this value is probably underestimated considering the limited frequency band (Nyquist frequency of 5 Hz). The large acceleration of CADO resembles another case where about 1 g was recorded at a fault damage zone [Seeber *et al.*, 2000; Ben-Zion *et al.*, 2003; Peng and Ben-Zion, 2006]. A similar acceleration was also recorded on a hill (Tarzana) during the  $M_w$  6.7 Northridge, California earthquake, and tentatively ascribed to topography and other local complexities [Spudich *et al.*, 1996]. However, a 3-D model of the Tarzana hill did not provide evidence of a clear dependence of the large acceleration on the local topographic features [Bouchon and Parker, 1996]. In our case we did not find a strong dependence of large amplitudes on the topography based on a simplified 2-D model. The strong directional amplification of the horizontal motion at CADO, which is seen also in the aftershock waveforms and the ambient noise record, may indicate some rock block vibrations. Such a model has been recently proposed to explain directional motions on unstable slopes in the southern Swiss Alps [Marzorati *et al.*, 2011; Moore *et al.*, 2011; Burjānek *et al.*, 2012]. However, the nearly harmonic motion at about 1 Hz of the CADO ground motion during the main shock suggests that a fault damage zone adjacent to the GPS station has a major role in explaining the observations through excitation of resonant waves in an underlying low-velocity zone.

### Acknowledgments

We are grateful to R. Devoti, M. Anzidei, A. Massucci, and S. Del Mese, who installed and maintained the 10 Hz sampling receiver at CADO before, during, and after the L'Aquila earthquake. This work has partially benefited from the activities performed in the NERA project (Network of European Research infrastructures for earthquake risk Assessment and mitigation, 262330), funded by the European Commission FP7 program, and in the FIRB-Abruzzo project, funded by the Italian Ministry of Education, University and Research. The Geopsy software used for the estimations of the Horizontal-over-Vertical spectral ratios has been developed within the framework of two EU-funded FP7 projects: SESAME, Site EffectS using AMBient Excitations (EESD project EVG1-CT-2000-00026); NERIES, NETwork of Research Infrastructures for European Seismology (026130). We also thank R. Cogliano, A. Fodarella, S. Pucillo, and G. Riccio; without their support the deployment of the seismic experiments would not have been possible. Deborah Di Naccio and Maurizio Vassallo helped us in the ambient noise measurements.

### References

- Anzidei, M., *et al.* (2009), Coseismic deformation of the destructive April 6, 2009 L'Aquila earthquake (central Italy) from GPS data, *Geophys. Res. Lett.*, *36*, L17307, doi:10.1029/2009GL039145.
- Atzori, S., I. Hunstad, M. Chini, S. Salvi, C. Tolomei, C. Biglioni, S. Stramondo, E. Trasatti, A. Antonoli, and E. Boschi (2009), Finite fault inversion of DInSAR coseismic displacement of the 2009 L'Aquila earthquake (central Italy), *Geophys. Res. Lett.*, *36*, L15305, doi:10.1029/2009GL039293.
- Avallone, A., M. Marzario, A. Cirella, A. Piatanesi, A. Rovelli, C. Di Alessandro, E. D'Anastasio, N. D'Agostino, R. Giuliani, and M. Mattone (2011), Very high rate (10Hz) GPS seismology for moderate-magnitude earthquakes: The case of the  $M_w$  6.3 L'Aquila (central Italy) event, *J. Geophys. Res.*, *116*, B02305, doi:10.1029/2010JB007834.
- Bagnaia, R., A. D'Epifanio, S. Sylos Labini (1992), Aquila and subaequan basins: An example of Quaternary evolution in central Apennines, *Italy Quat. Nova II*, 187e209.
- Bard, P. Y., H. Cadet, B. Endrun, M. Hobiger, F. Renalier, M. Theodulidis, D. Ohrnberger, F. Fäh, F. Sabetta, and P. Teves-Costa (2010), From non-invasive site characterization to site amplification: Recent advances in the use of ambient vibration measurements, *Earthquake Eng. Europe*, *17*(2), 105–123, doi:10.1007/978-90-481-9544-2\_5.
- Ben-Zion, Y., and K. Aki (1990), Seismic radiation from an SH line source in a laterally heterogeneous planar fault zone, *Bull. Seismol. Soc. Am.*, *80*, 971–994.
- Ben-Zion, Y. (1998), Properties of seismic fault zone waves and their utility for imaging low velocity structures, *J. Geophys. Res.*, *103*, 12,567–12,585.
- Ben-Zion, Y., Z. Peng, D. Okaya, L. Seeber, J. G. Armbruster, N. Ozer, A. J. Michael, S. Baris, and M. Aktar (2003), A shallow fault zone structure illuminated by trapped waves in the Karadere-Duzce branch of the North Anatolian Fault, western Turkey, *Geophys. J. Int.*, *152*, 699–717.
- Berg, S. S., and T. Skar (2005), Controls on damage zone asymmetry of a normal fault zone: Outcrop analyses of a segment of the Moab fault, SE Utah, *J. Struct. Geol.*, *27*(10), 1803e1822.
- Boncio, P., G. Lavecchia, and B. Pace (2004), Defining a model of 3D seismogenic sources for Seismic Hazard Assessment applications: The case of central Apennines (Italy), *J. Seismol.*, *8*, 407–425.
- Boncio, P., A. Pizzi, F. Brozzetti, G. Pomposo, G. Lavecchia, D. Di Naccio, and F. Ferrarini (2010), Coseismic ground deformation of the 6 April 2009 L'Aquila earthquake (central Italy,  $M_w$  6.3), *Geophys. Res. Lett.*, *37*, L06308, doi:10.1029/2010GL042807.
- Bouchon, M., and J. S. Parker (1996), Seismic response of a hill: The example of Tarzana, California, *Bull. Seismol. Soc. Am.*, *86*(1A), 66–72.
- Buech, F., T. R. Davies, and J. R. Pettinga (2010), The Little Red Hill seismic experimental study: Topographic effects on ground motion at a bedrock-dominated mountain edifice, *Bull. Seismol. Soc. Am.*, *100*, 2219–2229, doi:10.1785/0120090345.
- Burjānek, J., J. R. Moore, F. X. Yugsí Molina, and D. Fäh (2012), Instrumental evidence of normal mode rock slope vibration, *Geophys. J. Int.*, *188*, 559–569, doi:10.1111/j.1365-246X.2011.05272.x.
- Calderoni, G., A. Rovelli, and S. K. Singh (2013), Stress drop and source scaling of the 2009 L'Aquila earthquakes, *Geophys. J. Int.*, *192*, 260–274, doi:10.1093/gji/ggs011.
- Caserta, A., V. Ruggiero, and P. Lanucara (2002), Numerical modelling of dynamical interaction between seismic radiation and near surface geological structures: A parallel approach, *Comput. Geosci.*, *28*(9), 1069–1077.
- Çelebi, M., *et al.* (2010), Recorded motions of the 6 April 2009  $M_w$  6.3 L'Aquila, Italy, earthquake and implications for building structural damage: Overview, *Earthquake Spectra*, *26*(3), 651e684, doi:10.1193/1.3450317.
- Cheloni, D., *et al.* (2010), Coseismic and initial postseismic slip of the 2009  $M_w$  6.3 L'Aquila earthquake, Italy, from GPS measurements, *Geophys. J. Int.*, *181*, 1539–1546, doi:10.1111/j.1365-246X.2010.04584.x.
- Chiarabba, C., L. Jovane, and R. Di Stefano (2005), A new view of Italian seismicity using 20 years of instrumental recordings, *Tectonophysics*, *395*, 251–268, doi:10.1016/j.tecto.2004.09.013.
- Chiarabba, C., *et al.* (2009), The 2009 L'Aquila (central Italy)  $M_w$  6.3 earthquake: Main shock and aftershocks, *Geophys. Res. Lett.*, *36*, L18308, doi:10.1029/2009GL039627.
- Chiaraluce, L., L. Valoroso, D. Piccinini, R. Di Stefano, and P. De Gori (2011), The anatomy of the 2009 L'Aquila normal fault system (central Italy) imaged by high resolution foreshock and aftershock locations, *J. Geophys. Res.*, *116*, B12311, doi:10.1029/2011JB008352.
- Cirella, A., A. Piatanesi, M. Cocco, E. Tinti, L. Scognamiglio, A. Michelini, A. Lomax and E. Boschi (2009), Rupture history of the 2009 L'Aquila (Italy) earthquake from non-linear joint inversion of strong motion and GPS data, *Geophys. Res. Lett.*, *36*, L19304, doi:10.1029/2009GL039795.
- Cirella, A., A. Piatanesi, E. Tinti, M. Chini, and M. Cocco (2012), Complexity of the rupture process during the 2009 L'Aquila, Italy, earthquake, *Geophys. J. Int.*, *190*, 607–621, doi:10.1111/j.1365-246X.2012.05505.x.
- Civico, R., S. Pucci, D. Pantosti and P. M. De Martini (2013), Morphotectonic analysis of the long-term surface expression of the Paganica-San Demetrio Fault System (2009 L'Aquila earthquake, Central Italy), *Geophys. Res. Abs.*, *15*, EGU2013-11372-1.

- D'Agostino, N., S. Mantenuto, E. D'Anastasio, R. Giuliani, M. Mattone, S. Calcaterra, P. Gambino, and L. Bonci (2011), Evidence for localized active extension in the central Apennines (Italy) from Global Positioning System observations, *Geology*, *39*, 291–294, doi:10.1130/G31796.1.
- D'Agostino, N., D. Cheloni, G. Fornaro, R. Giuliani, and D. Reale (2012), Space-time distribution of afterslip following the 2009 L'Aquila earthquake, *J. Geophys. Res.*, *117*, B02402, doi:10.1029/2011JB008523.
- Di Stefano, R., C. Chiarabba, L. Chiaraluze, M. Cocco, P. De Gori, D. Piccinini and L. Valoroso (2011), Fault zone properties affecting the rupture evolution of the 2009 ( $M_w$  6.1) L'Aquila earthquake (central Italy): Insights from seismic tomography, *Geophys. Res. Lett.*, *38*, L10310, doi:10.1029/2011GL047365.
- EMERGEO Working Group (2009), Evidence for surface rupture associated with the  $M_w$  6.3 L'Aquila earthquake sequence of April 2009 (central Italy), *Terra Nova*, *22*, 43–51, doi:10.1111/j.1365-3121.2009.00915.x.
- Foglio CARG 1:50,000 (2009), Cartografia geologica ufficiale. Foglio CARG 1:50,000 N. 359, L'Aquila.
- Fohrmann, M., H. Igel, G. Jahnke, and Y. Ben-Zion (2004), Guided waves from sources outside faults: An indication for shallow fault zone structure?, *Pure Appl. Geophys.*, *161*, 2125–2137, doi:10.1007/s00024-004-2553-y.
- Galadini, F. (1999), Pleistocene change in the central Apennine fault kinematics, a key to decipher active tectonics in central Italy, *Tectonics*, *18*, 877–894.
- Galli, P., F. Galadini, and D. Pantosti (2008), Twenty years of paleoseismology in Italy, *Earth Sci. Rev.*, *88*(1–2), 89–117, doi:10.1016/j.earscirev.2008.01.001.
- Geli, L., P.-Y. Bard, and B. Jullien (1988), The effect of topography on earthquake ground motion: A review and new results, *Bull. Seismol. Soc. Am.*, *78*, 42–63.
- Ghisetti, F., and L. Vezzani (1997), Interfering paths of deformation and development of arcs in the fold-and-thrust belt of the central Apennines (Italy), *Tectonics*, *16*(3), 523–536, doi:10.1029/97TC00117.
- Improta, L., et al. (2012), High-resolution controlled-source seismic tomography across the Middle Aterno basin in the epicentral area of the 2009,  $M_w$  6.3, L'Aquila earthquake (central Apennines, Italy), *Italian J. Geosci.*, *131*(3), 373–388, doi:10.3301/IJG.2011.35.
- Konno, K., and T. Ohmachi (1998), Ground-motion characteristics estimated from spectral ratio between horizontal and vertical components of microtremor, *Bull. Seismol. Soc. Am.*, *88*, 228–241.
- Lee, S.-J., Y.-C. Chan, D. Komatitsch, B.-S. Huang, and J. Tromp (2009), Effects of realistic surface topography on seismic ground motion in the Yangminshan region of Taiwan based upon the spectral-element method and LiDAR DTM, *Bull. Seismol. Soc. Am.*, *99*, 681–693, doi:10.1785/0120080264.
- Marzorati, S., C. Ladina, E. Falucci, S. Gori, M. Saroli, G. Ameri, and F. Galadini (2011), Site effects “on the rock”: The case study of Castelvecchio Subequo (L'Aquila, central Italy), *B. Earthquake Eng.*, *9*, 841–868, doi:10.1007/s10518-011-9263-5.
- Moore, J. R., V. Gischig, J. Burjanek, S. Loew, and D. Fäh (2011), Site effects in unstable rock slopes: Dynamic behavior of the Randa instability (Switzerland), *Bull. Seismol. Soc. Am.*, *101*(6), 3110–3116, doi:10.1785/0120110127.
- Peng, Z., and Y. Ben-Zion (2006), Temporal changes of shallow seismic velocity around the Karadere-Duzce branch of the north Anatolian fault and strong ground motion, *Pure Appl. Geophys.*, *163*, 567–600, doi:10.1007/s00024-005-0034-6.
- Pischiutta, M., G. Cultrera, A. Caserta, L. Luzi, and A. Rovelli (2010), Topographic effects on the hill of Nocera Umbra, central Italy, *Geophys. J. Int.*, *182*, 977–987, doi:10.1111/j.1365-246X.2010.04654.x.
- Roberts, G., and A. M. Michetti (2004), Spatial and temporal variations in growth rate along active normal fault systems: An example from the Lazio Abruzzo Apennines, central Italy, *J. Struct. Geol.*, *26*, 339–376, doi:10.1016/S0191-8141(03)00103-2.
- Rovelli, A., F. Cara, C. Cornou, G. Di Giulio, C. Guyonnet-Benaize, G. Milana, A. Savvaidis, N. Theodulidis (2013), Network of European Research Infrastructures for Earthquake Risk Assessment and Mitigation, Deliverable D11.3, Geophysical surveys on basins and topographies: Report and findings, EC Project n. 262330, <http://www.nera-eu.org/>.
- Ruggiero, V., P. Lanucara, M. P. Busico, A. Caserta, and B. Firmani (2004), Numerical modelling of the ground motion: A parallel approach for finite element methods, in *Proceedings of the 7th Conference on Applied and Industrial Mathematics in Italy*, pp. 487–495, World Scientific, Venice, Italy.
- Santoni, D., C. Giuffrida, V. Ruggiero, A. Caserta, and P. Lanucara (2004), Web user-friendly interface to produce input data for numerical simulations of seismic wave propagation problem, *Geophys. Res. Abs.*, *6*, 06,020.
- Scognamiglio, L., E. Tinti, A. Michelini, D. S. Dreger, A. Cirella, M. Cocco, S. Mazza, and A. Piatanesi (2010), Fast determination of moment tensors and rupture history: What has been learned from the 6 April 2009 L'Aquila earthquake sequence, *Seismol. Res. Lett.*, *81*(6), 892–906, doi:10.1785/gssrl.81.6.892.
- Seeber, L., J. G. Armbruster, N. Ozer, M. Aktar, S. Baris, D. Okaya, Y. Ben-Zion, and E. Field (2000), The 1999 Earthquake Sequence along the North Anatolia Transform at the Juncture between the Two Main Ruptures, in *The 1999 Izmit and Duzce Earthquakes: Preliminary Results*, edited by A. Barka et al., pp. 209–223, ITU Publications, Istanbul Technical Univ. Press, Istanbul, Turkey.
- Serpelloni, E., L. Anderlini, and M. E. Belardinelli (2012), Fault geometry, coseismic-slip distribution and Coulomb stress change associated with the 2009 April 6,  $M_w$  6.3, L'Aquila earthquake from inversion of GPS displacements, *Geophys. J. Int.*, *188*, 473–489, doi:10.1111/j.1365-246X.2011.05279.x.
- Spudich, P., M. Hellweg, and W. H. K. Lee (1996), Directional topographic site response at Tarzana observed in aftershocks of the 1994 Northridge, California, earthquake: Implications for mainshock motions, *Bull. Seismol. Soc. Am.*, *86*(1B), S193–S208.
- Trasatti, E., C. Kyriakopoulos, and M. Chini (2011), Finite element inversion of DInSAR data from the  $M_w$  6.3 L'Aquila earthquake, 2009 (Italy), *Geophys. Res. Lett.*, *38*, L08306, doi:10.1029/2011GL046714.
- Valoroso, L., L. Chiaraluze, D. Piccinini, R. Di Stefano, D. Schaff, and F. Waldhauser (2013), Radiography of a normal fault system by 64,000 high-precision earthquake locations: The 2009 L'Aquila (central Italy) case study, *J. Geophys. Res. Solid Earth*, *118*, 1156–1176, doi:10.1002/jgrb.50130.
- Walters, R. J., J. R. Elliott, N. D'Agostino, P. C. England, I. Hunstad, J. A. Jackson, B. Parsons, R. J. Phillips, and G. Roberts (2009), The 2009 L'Aquila earthquake (central Italy): A source mechanism and implications for seismic hazard, *Geophys. Res. Lett.*, *36*, L17312, doi:10.1029/2009GL039337.
- Working Group Catalogo Parametrico dei Terremoti Italiani (CPTI) (2004), Catalogo Parametrico dei Terremoti Italiani, v. 2004 (CPTI04), 320 pp., Istituto Nazionale di Geofisica e Vulcanologia, Bologna, Italy [Available at <http://emidius.mi.ingv.it/CPTI/>].